ChemComm

COMMUNICATION

Electronic Supporting Information (ESI)

Light intensity–directed selective CO_2 photoreduction using iron(0)–zirconium dioxide photocatalyst

Tomoki Oyumi,[a] Ikki Abe,[a] Masahito Sasaki,[a] and Yasuo Izumi*[a]

1. Introduction

First-row transition metals such as Ti, V, Cr, Mn, Fe, Co, and Ni present promising inexpensive alternatives as photocatalytic active components for CO_2 reduction, potentially replacing currently preferred but expensive Cu, Ag, and Pt metals.[S1,S2]

Table S1 Reported photocatalysts that utilize Fe as active sites.

Entry	Photocatalyst	Reducing agent	Product	Formation rate	Ref.
a	Fe–MIL-100	TEOA	Formate	150 μmol h^{-1} g_{cat}^{-1}	S3
b	g-C_3N_4–Fe-MIL-88B		CO	13 μmol h^{-1} g_{cat}^{-1}	S4
c	FeO_x–In_2O_3		CO	4.8 mmol h^{-1} g_{cat}^{-1}	S5
d	Fe-TCPP–MOF		CO	10 mmol h^{-1} g_{cat}^{-1}	S6
e	Fe-N-MIL-101-rGO	H_2O			S7
f	Fe–Ti-MXene	H_2O	CO	260 μmol h^{-1} g_{cat}^{-1}	S8
g	g-C_3N_4–Fe-PCN-222		CO		S9
h	Fe–TiO_2		CO, CH_4	21 μmol h^{-1} g_{cat}^{-1}, 40 μmol h^{-1} g_{cat}^{-1}	S10
i	FeO_x–MOF		CO	170 μmol h^{-1} g_{cat}^{-1}	S11
j	Fe–COF	H_2O	CO	4.0 mmol h^{-1} g_{cat}^{-1}	S12
k	Fe–bpy–COF	BIH	Formate, CO	4.1 mmol h^{-1} g_{cat}^{-1}, 2.1 mmol h^{-1} g_{cat}^{-1}	S13
l	Fe_2O_3–Ti MXene	H_2O	CO	240 μmol h^{-1} g_{cat}^{-1}	S14
m	Fe-N_3tpy	TEA	CO	6.2 mmol h^{-1} g_{cat}^{-1}	S15
n	Fe_2O_3@In_2S_3	H_2O	CO	43 μmol h^{-1} g_{cat}^{-1}	S16
o	NH_2-MIL-101(Fe)@Ti_3C_2		CO	56 μmol h^{-1} g_{cat}^{-1}	S17
p	NH_2-MIL-101(Fe)@Bi_2MoO_6	TEOA	CO	67 μmol h^{-1} g_{cat}^{-1}	S18
q	Fe/Ti-BPDC MOF		HCO_2H	700 μmol g^{-1} h^{-1}	S19
r	Fe_3 oxide–MOF	IPA	CO	140 μmol h^{-1}	S20
s	Fe–Bi_5O_7I	H_2O	CO	12 μmol·g^{-1}·h^{-1}	S21
t	Fe–Bi_2O_2S		CH_4	1.7 μmol g^{-1} h^{-1}	S22
u	Ferrocene–Ti cluster	TEOA	Formate	40 μmol g^{-1} h^{-1}	S23
v	Fe(BPAbipy)	BIH	CO	52 μmol h^{-1}	S24

2. Experimental section

The Fe^0-photocatalyst was synthesized via the following procedure. ZrO_2 (0.50 g, specific surface area: 100.5 m^2 g^{-1}; Type JRC-ZRO-7, Catalysis Society of Japan) was dispersed in deionized water (100 mL; conductivity <0.055 μS cm^{-1}, model RFU424TA, Advantec, Japan) along with $Fe(NO_3)_3$·$9H_2O$ (0.2935 g). The suspension was ultrasonicated for 20 min before the dropwise addition of $NaBH_4$ (0.3298 g) dissolved in deionized water (20 mL) over 5 min. Major impurity of the ZrO_2 sample was Hf: 0.55 wt% in sample based on our X-ray absorption spectroscopy study. The reaction mixture was

[a] Department of Chemistry, Graduate School of Science, Chiba University, Yayoi 1-33, Inage-ku, Chiba 263-8522, Japan.

stirred at 900 rotations per minute (rpm) for 10 min, followed by filtration using a membrane filter (pore size = 0.1 µm; Omnipore Type JVWP04700, Merck–Millipore, Darmstadt, Germany) and washed five times with deionized water (50 mL). The resulting solid was initially dried at 373 K for 12 h, then further dried at 373 K for an additional 24 h. Finally, the sample was heated under H_2 (21.7 kPa) at 973 K for 1 h. The obtained photocatalyst is referred to as Fe^0 (7.5 wt %)–ZrO_2-973R.

CO photoreduction tests at the gas/solid interface were performed using 20 mg of the photocatalyst. The reaction was conducted in the presence of $^{13}CO_2$ (2.3 kPa, chemical purity >99.9%; 99.0% ^{13}C, 0.1% ^{17}O, 0.7% ^{18}O, Cambridge Isotope Laboratories, Inc., Tewksbury, MA, USA) and H_2 (2.3–21.7 kPa, purity >99.99%). The photocatalyst was placed in a U-shaped quartz reactor and irradiated with ultraviolet–visible (UV–Vis) light from a 300 W Xe arc lamp (Model MAX 350, Asahi Spectra, Japan) via a quartz light guide (diameter: 5 mm).[S25] The distance between the fiber light exit and the photocatalyst was maintained at 2 cm. The light intensity at the center of the sample was adjusted between 110 and 472 mW cm^{-2} (Table 1a–d', main text). CO_2 photoreduction tests were also performed by cooling the quartz reactor with 2.5 L water in quartz bath (Chart S1).

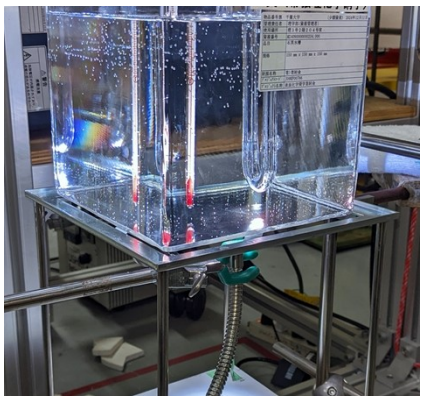

Chart S1 A picture of CO_2 photoreduction test by cooling the quartz reactor with 2.5 L water in quartz bath.

Online gas chromatography–mass spectrometry (GC–MS) analysis was performed using a JMS-Q1050GC (JEOL, Japan). A packed column of 13X-S molecular sieves (length: 3 m, internal diameter: 3 mm; GL Sciences, Inc., Japan) was used, with He (purity >99.99995%) as the carrier gas. The ionization energy of the separated gas was 20 eV. Detection of $^{13}CH_4$ and $^{12}CH_4$ relied was based on their mass-to-charge ratios (m/z): $^{13}CH_4$ at m/z = 17 and $^{12}CH_4$ at m/z = 16. The fragment ratio of CH_3^+: CH_4^+ was 0.708:1. Similarly, ^{13}CO was identified at m/z = 29, $^{13}C_2H_6$ and $^{13}C_2H_4$ at m/z = 30 as $^{13}C_2H_4$ fragment, $^{13}C_3H_8$ at m/z = 31 as $^{13}C_2H_5^+$ fragment, and $^{13}C_3H_6$ at m/z = 44 as $^{13}C_3H_5^+$ fragment. All reactants and products were uniquely quantified based on their GC retention times in the mass chromatogram.

CO_2 photoconversion tests were conducted using CO_2 (95 kPa) and H_2O (70 mL) with $NaHCO_3$ (0.203 g, purity >99.5%; Wako Pure Chemical, Japan) dissolved in the solution. Photocatalyst samples (2.7 mg), pretreated under H_2 were sealed by flame and transferred to a Pyrex flask reactor under an Ar atmosphere using the Schlenk technique. CO_2 (95 kPa) was circulated within a closed Pyrex glass system connected to the Pyrex flask, which was equipped with a quartz window containing the photocatalyst. The reactor was irradiated with UV–Vis light from a Model MAX-350 through a quartz light guide. The distance between the fiber light exit and the quartz window was 2 cm. The integrated light intensity for the suspended sample was measured at 367 mW per flask (Table 1e and e'). The suspension was stirred at 1,000 rpm, and the reaction gas was continuously bubbled using a gas circulation pump connected to the reactor during the photocatalytic reaction tests. Product analysis was performed using an online GC–thermal conductivity detector (Model GC-8AT, Shimadzu, Kyoto, Japan) equipped with a packed column of 13X-S molecular sieves (length: 3 m, internal diameter: 3 mm). Additionally, GC–MS analysis was conducted using a packed column of 13X-S molecular sieves, with He (purity >99.99995%) as the carrier gas in both cases.

UV–Vis spectra were recorded using a double-beam V-650 spectrometer (JASCO, Tokyo, Japan) equipped with D_2 and halogen lamps for measurements below and above 340 nm, respectively. A photomultiplier tube and an integrated ISV-469 sphere were used for diffuse reflectance detection in the 200–800 nm range. Samples pretreated under H_2 were transferred to an airtight cell using a vacuum-type glove box (UN-6509LCIY, Unico, Japan) under an Ar atmosphere. A polytetrafluoroethylene plate was used as the reference. Absorption and fluorescence spectra were recorded using an FP-8600 spectrometer (JASCO; Chiba Iodine Resource Innovation Center, Chiba University, Japan) equipped with a 150 W Xe arc lamp (Type UXL-159, Ushio, Japan) and a photomultiplier tube. Excitation was performed at 200 nm, and fluorescence emission was measured in the 300–800 nm range. The incident excitation light from the Xe lamp was monitored using a Si photodiode, and the detected fluorescence was normalized based on the incident light intensity at each wavelength. The photocatalyst powder (2.0 mg) was dispersed in deionized water (< 0.055 µS cm^{-1}; 3.0 mL) and ultrasonicated (430 W, 38 kHz) for 30 min. All spectra were recorded for the suspensions in a quartz cell at 295 K.

Fe K-edge X-ray absorption fine structure spectra were measured at beamline 9C of the Photon Factory, High Energy Accelerator Research Organization, Tsukuba, Japan. A Si (1 1 1) double-crystal monochromator was used to analyze X-rays emitted from the storage ring via a bending magnet. The monochromator was adjusted using a piezo transducer and focused using a bent cylindrical mirror coated with Rh. Photocatalyst samples were pretreated in a quartz U-tube and transferred to a Pyrex cell filled with reaction gas (CO_2 + H_2). The cell was equipped with polyethylene terephthalate film (Toyobo, Japan, Type G2, 50 µm thick) on both sides. A 300 W Xe arc lamp (Model MAX 350) served as the light source, with a fiber light exit positioned 3 cm from the photocatalyst (322 mW cm^{-2}).

X-ray diffraction patterns were recorded using a D8 ADVANCE diffractometer (Bruker, Billerica, MA, USA) at the Center for Analytical Instrumentation, Chiba University. The measurements

were conducted over a Bragg angle range of $2\theta_B$ = 10°–80°, with a scan step of 0.02° and a scan rate of 0.5 s per step. The instrument operated at 40 kV and 40 mA, utilizing Cu Kα radiation (λ = 0.15419 nm) with a Ni filter.

In situ FTIR spectroscopy measurements were conducted at 295 K using a model FT/IR-4200 spectrometer (JASCO, Tokyo, Japan) over a spectral range of 4000–650 cm^{-1}. The Fe (7.5 wt%)–ZrO_2 photocatalyst disk (60 mg), mixed with an equal amount of ZrO_2 (60 mg), was pretreated under H_2 at 973 K in a quartz cell and subsequently transferred to an FTIR cell under an Ar atmosphere using a vacuum-type glove box (UN-6509LCIY). A mixed gas of $^{13}CO_2$ (2.3 kPa) and H_2 (21.7 kPa) was introduced to the photocatalyst disk. The sample was then irradiated with UV–Vis light from a 300 W Xe arc lamp (Model MAX 350) via a quartz fiber light guide. Finally, the FTIR cell containing the photocatalyst disk was evacuated using rotary and diffusion pumps (10^{-6} Pa). The fiber light exit was positioned 3 cm from the sample disk, with an incident light intensity of 265 mW cm^{-2}. The spectrometer was set to an energy resolution of 1 cm^{-1}, and data accumulation was performed over 512 scans (~2 s per scan).

Spin-polarized periodic density functional (DFT) theory calculations were performed using the Vienna Ab initio Simulation Package code version 6.4.2[S26] on a WJ9J-W231 server equipped with an Intel Xeon w9-3495X processor (1.9 GHz, 56 cores; Tsukumo, Japan). Additionally, part of the computations was conducted using the supercomputer facilities at the Institute for Solid State Physics, University of Tokyo, Japan. The projector-augmented wave method was applied at the DFT-D3 level to account for van der Waals interactions. The generalized gradient approximation-revised Perdew–Burke–Ernzerhof exchange-correlation functional was utilized, with a plane-wave energy cutoff set at 500 eV.

The convergence criterion was set at 10^{-4} eV for the self-consistent field cycle, and structural optimizations were considered converged when the forces on all atoms were smaller than 1.0 eV nm^{-1}. All atoms were fully relaxed during structural optimization. The Brillouin zone was sampled using a 3 × 3 × 1 wave number vector *k*-point grid. The (1 1 1) surface of body-centered cubic Fe was modeled using a 3 × 3 × 2 unit cell slab, with a vacuum spacing of 1.5 nm between slabs.[S27]

The adsorption energy (E_{ads}) of CO_2 was calculated based on eq. S1.

$$E_{ads} = E_{mol/slab} - E_{mol} - E_{slab}, \quad \text{(S1)}$$

where $E_{mol/slab}$ is the total energy of the adsorbate on the slab surface, and E_{mol} and E_{slab} are the energies of an isolated molecule in the gas phase and of the surface, respectively.

3. Results and discussion

3-1. Photocatalytic CO_2 reduction tests

The ^{13}CO formation rate using Fe (7.5 wt%)–ZrO_2-973R photocatalyst @110 mW cm^{-2} until 5 h of photoreaction under $^{13}CO_2$ (2.3 kPa) and H_2 (21.7 kPa; 3.7 μmol h^{-1} g_{cat}^{-1}; Table 1a) corresponds 0.37 μmol of ^{13}CO at 5 h. This exceeds the evaluated surface O vacancies ($V_O^{\bullet\bullet}$) population: 0.070 μmol per 20 mg of photocatalyst (Table S3g and Fig. S7), and suggests that ^{13}CO was photocatalytically formed rather than stoichiometric reaction of CO_2 and $V_O^{\bullet\bullet}$ to form CO filling in the O vacancy.

A photocatalytic reduction test of CO_2 was performed in comparison to tests listed in Table 1 to verify H_2 pressure dependence. $^{13}CO_2$: H_2 ratio was 1: 9.4 in Table 1 while CO_2 (or CO): H_2 ratio was 1: (1–6) in tests in Table S4, except for reference S40. Therefore, a test at $^{13}CO_2$: H_2 ratio of 1: 1 was performed irradiated by light at 473 mW cm^{-2} (Table S2b and b'). In comparison to the test using $^{13}CO_2$ and H_2 with the ratio 1: 9.4 (entries c and c'), the formation rate of $^{13}CO_2$ was suppressed to 40% while that of $^{13}CH_4$ became 1.0% of rates under higher H_2 pressure. Thus, H_2 pressure dependence suppressed the progress of sequential reaction steps from CO_2 to CO then CH_4 (Scheme 1a).

Next, a reference photocatalytic test was also performed using ZrO_2 reduced at 973 K under H_2 (Table S2a). The ^{13}CO formation rate (1.7 μmol h^{-1} g_{cat}^{-1}) was significantly lower compared to initial $^{13}CH_4$ formation rate under similar photocatalytic reaction conditions (Table 1b). Furthermore, no trend was found between reduction temperature of photocatalyst under H_2 and the amount of chemisorbed CO_2 (Table S3), corresponding to O vacancy on the ZrO_2 surface. Thus, noncatalytic CO_2 reduction to CO by the reaction of $V_O^{\bullet\bullet}$ on ZrO_2 created by reduction at high temperature under H_2 was minimal in this study.

In the photocatalytic test using CO_2 and H_2O (Fig. S1), sequential trend of primary water photosplitting was observed as the quick O_2 evolution and secondary CO then CH_4 generation. This trend suggested the inclusion of reverse water–gas shift reaction step (eq. S3).

$2H_2O \rightarrow 2H_2 + O_2$ (S2)
$CO_2 + H_2 \rightarrow CO + H_2O$ (S3)
$CO + 3H_2 \rightarrow CH_4 + H_2O$ (S4)

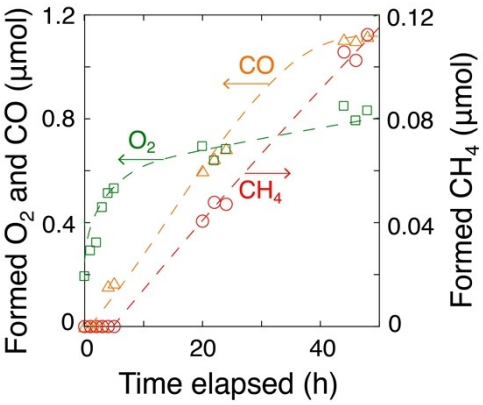

Fig. S1 Time course of CO, CH_4, and O_2 formation using Fe^0 (7.5 wt%)–ZrO_2-973R photocatalyst, with CO_2 (95 kPa), H_2O (70 mL), and UV–Vis light irradiation at 367 mW per cell. The O_2 amount was corrected by subtracting the N_2 amount multiplied by 20.9/78.1 at each time.

Table S2 CO_2 photoreduction outcomes using ZrO_2 and Fe (7.5 wt%)–ZrO_2 both prereduced at 973 K in the presence of H_2.

Entry	Catalyst	$^{13}CO_2$	H_2	Light intensity (mW cm^{-2})	Stage of reaction test (h)	Formation rate (μmol h^{-1} g_{cat}^{-1})				
						^{13}CO	$^{13}CH_4$	$^{13}C_2H_6$	$^{13}C_3H_8$	O_2
a	ZrO_2	2.3 kPa	21.7 kPa	257	0–48	1.7	<0.002	<0.002	<0.002	<0.002
b	Fe (7.5 wt%)–ZrO_2		2.3 kPa	473	0–5	27.7	1.75	0.0511		
b′					5–48	13.4	0.213	0.0302		
c			21.7 kPa	472	0–5	69	170	2.1	0.30	
c′					5–48	18	20	2.3	0.56	

Entries c and c′ are the same as Table 1c and c′ for comparison to entries b and b′.

Table S3 Chemisorbed amount of CO_2 during the photoexchange using ZrO_2, Ag (5.0 wt%)–ZrO_2, Au (5.0 wt%)–ZrO_2, Ni (10 wt%)–ZrO_2, Co (7.5 wt%)–ZrO_2, and Fe (7.5 wt%)–ZrO_2 under UV–visible light irradiation

Entry	$^{13}CO_2$ (kPa)	Catalyst		Reduction tempeature (K)	Chemisorbed CO_2 (μmol)	Reference
		Type	Amount (mg)			
a	0.67	ZrO_2	100	–	2.3	S45
b		ZrO_2	20	723	0.66	S46
c		Ag (5.0 wt%)–ZrO_2	100	–	3.5	S45
d		Au (5.0 wt%)–ZrO_2		–	2.9	S47
e		Ni (10 wt%)–ZrO_2	20	723	0.54	S46
f	0.68	Co (7.5 wt%)–ZrO_2		823	0.050	S25
g	0.69	Fe (7.5 wt%)–ZrO_2		973	0.070	This work

Table S4 Reported thermal catalysts that utilize Fe as active sites for CO_2 and/or CO hydrogenation into hydrocarbon(s).

Entry	Catalyst	$T_{reduction}$ (K)	Fe state	$T_{reaction}$ (K)	Reactant	Product	Formation rate	Ref.
a	Fe–CeO_2	673	Fe^{2+}, Fe^{3+}	623	CO_2	CH_4	26 mmol h^{-1} g_{Fe}^{-1}	S29
b	Fe–$Ce_{0.1}Zr_{0.9}O_2$	573 (Ar)		573–773				S30
c	Fe–SiO_2	623	γ-Fe_2O_3	673			0.97 mol h^{-1} mol_{Fe}^{-1}	S31
d	Fe–CeO_2–Al_2O_3	1023	Fe, Fe_2O_3 and Fe_3O_4	683			6.2 mmol h^{-1} g_{cat}^{-1}	S32
e	Fe–mesoporous SiO_2	623	Fe^{3+}	773			0.99 mmol h^{-1} g_{cat}^{-1}	S33
f	Fe–mesoporous SiO_2	773		623			35 mol h^{-1} mol_{Fe}^{-1}	S34
g	$Fe^{II}(Fe^{III}_{0.5}Al_{0.5})_2O_4$		Fe_5C_2, Fe_7C_3, Fe oxide	593			2.6 μmol h^{-1} g_{cat}^{-1}	S35
h	Fe–Al_2O_3		Fe^{2+}, Fe^{3+}	673		$C_{1–12}$ HC	0.14 mol h^{-1} g_{Fe}^{-1}	S36
	Fe–C						0.068 mol h^{-1} g_{Fe}^{-1}	
i	$Fe^{II}(Fe^{III}_{0.5}Al_{0.5})_2O_4$		Fe_5C_2, Fe_7C_3, Fe oxide	593		CH_4	46 mmol h^{-1} g_{cat}^{-1}	S37
						$C_{2–4}$ HC	62 mmol h^{-1} g_{cat}^{-1}	
j	$Fe(Fe_{0.5}Al_{0.5})_2O_4$		Fe_5C_2, Fe_7C_3, Fe oxide	593		CH_4	46 mmol h^{-1} g_{cat}^{-1}	S38
k	Fe–SiO_2			623			0.52 mmol h^{-1} g_{Fe}^{-1}	S39
				663	CO		1.4 mmol h^{-1} g_{Fe}^{-1}	
l	Blast furnace sludge (Fe rich)	773	Fe_2O_3, Fe_3O_4	593			0.16 mmol h^{-1} g_{cat}^{-1}	S40
m	Fe–Zn oxide	613 (Ar)	Fe_2C, Fe_5C_2	613		$C_{1–5}$ HC	5.0 mol h^{-1} g_{Fe}^{-1}	S41
n	Fe–C	none		548			2.5 mmol h^{-1} g_{cat}^{-1}	S42
		673					4.1 mmol h^{-1} g_{cat}^{-1}	

3-2. Charactrizations

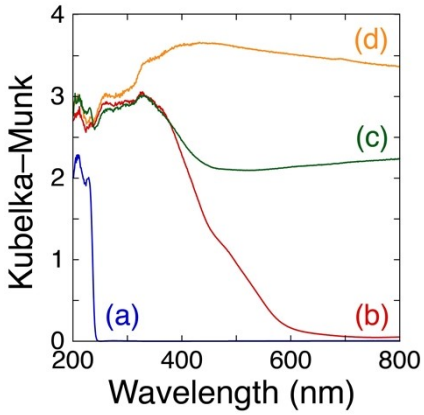

Fig. S2 Diffuse-reflectance UV–Vis absorption spectra for (a) ZrO_2, (b) incipient Fe_3O_4–ZrO_2, (c) Fe^0 (7.5 wt%)–ZrO_2-973R, and (d) Fe^0 (7.5 wt%)–ZrO_2-973R after a 48-h photocatalytic $^{13}CO_2$ reduction test.

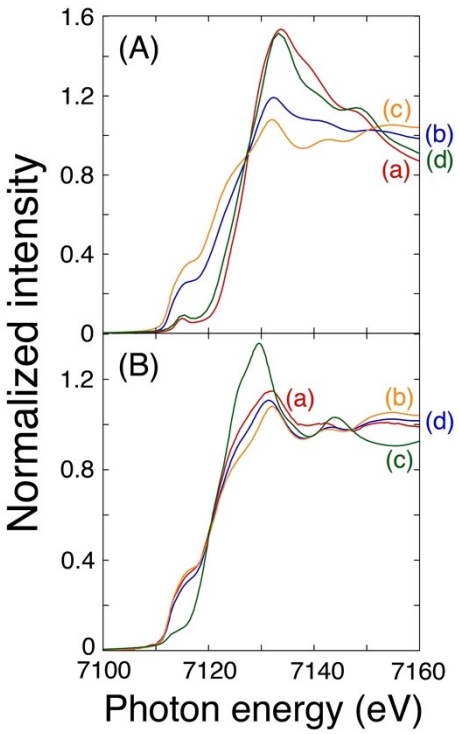

Fig. S3 Normalized Fe K-edge X-ray absorption near-edge structures for (A) (a) incipient Fe_3O_4–ZrO_2, (b) Fe^0 (5.0 wt%)–ZrO_2 reduced at 973 K, (c) standard Fe^0 metal, and (d) Fe_3O_4;[S28] and (B) (a) Fe^0 (7.5 wt%)–ZrO_2-973R under CO_2 (2.3 kPa) and H_2 (21.7 kPa) in the dark, (b) standard Fe^0 metal, (c) FeO, and (d) the convolution spectrum of Fe^0 metal and FeO with a mixing ratio of 8: 2.

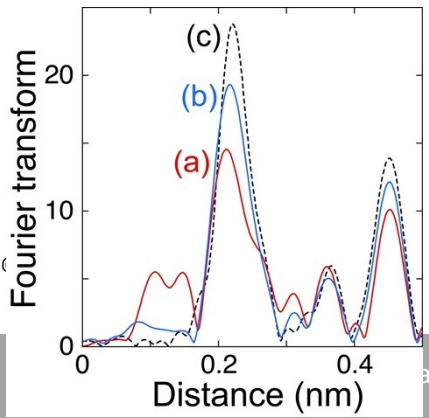

Fig. S4 Fourier transform of angular wave number k^3-weighted Fe K-edge extended X-ray absorption fine structure measured for (a) Fe^0 (5.0 wt%)–ZrO_2 and (b) Fe^0 (20 wt%)–ZrO_2, both reduced under H_2 at 973 K, and (c) Fe^0 foil (thickness 4 μm).

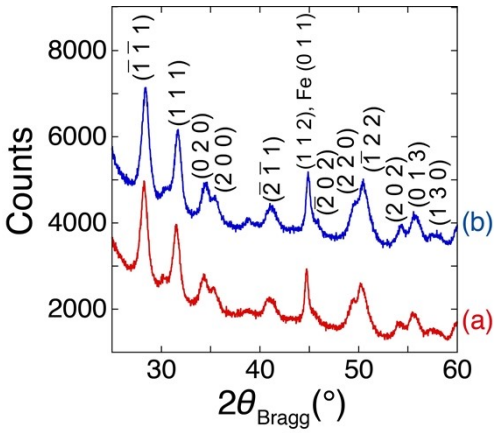

Fig. S5 X-ray diffraction pattern for (a) Fe^0 (7.5 wt%)–ZrO_2-973R and (b) Fe^0 (7.5 wt%)–ZrO_2-973R after a 48-h photocatalytic $^{13}CO_2$ reduction test.

Interband emission peaks may be owing to elemental impurity energy level[S43] as well as impurity energy level (Fig. S6; see main text). The major impurity in ZrO_2 employed was HfO_2: Hf/(Zr + Hf) ratio was 0.77 wt% (see the Experimental section). A part of the peak at 468 nm in Fig. S6 may be owing to HfO_2.[S44]

The $^{13}CO_2$ exchange test using Fe^0 (7.5 wt%)–ZrO_2 showed quick adsorption of $^{13}CO_2$ (99%) and $^{12}CO_2$ (1%) (in total 20 μmol) followed by gas temperature increase (gas expansion) simulated by sigmoid function as well as slower adsorption of CO_2 (in total 4.1 μmol). The remaining term of relatively quick $^{12}CO_2$ increase (0.070 μmol; Table S3g and Fig. S7) suggested preadsorbed $^{12}CO_2$ on $V_O^{\bullet\bullet}$ site.[S25,S45–S47] Based on this amount, surface $V_O^{\bullet\bullet}$ sites were evaluated to one per 44 nm^2 (see main text).

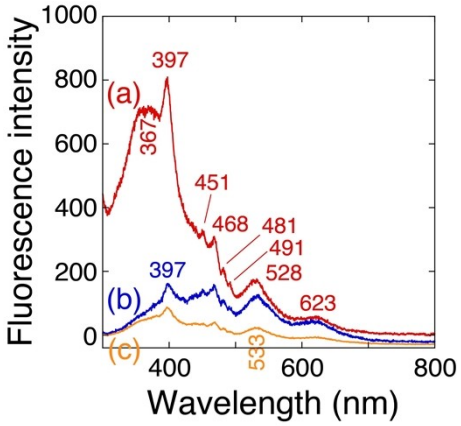

Fig. S6 UV–Vis fluorescence emission spectra for (a) ZrO_2, (b) incipient Fe_3O_4–ZrO_2, and (c) Fe^0 (7.5 wt%)–ZrO_2-973R at an excitation wavelength of 200 nm.

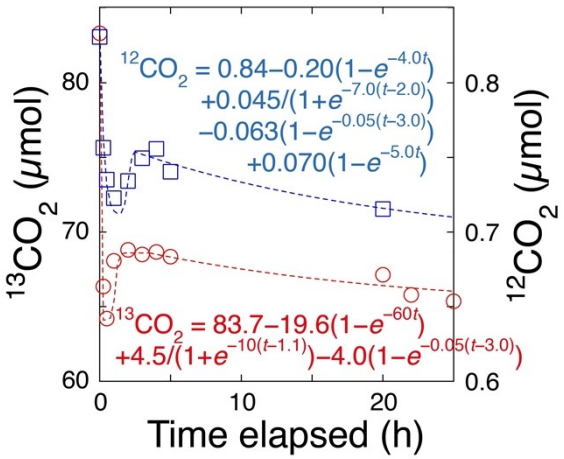

Fig. S7 Time course of $^{13}CO_2$ (0.69 kPa) exchange reaction using Fe^0 (7.5 wt%)–ZrO_2-973R (20 mg) irradiated by UV–visible light (270 mW cm^{-2}). Temperature change upon light irradiation was simulated by sigmoid function.

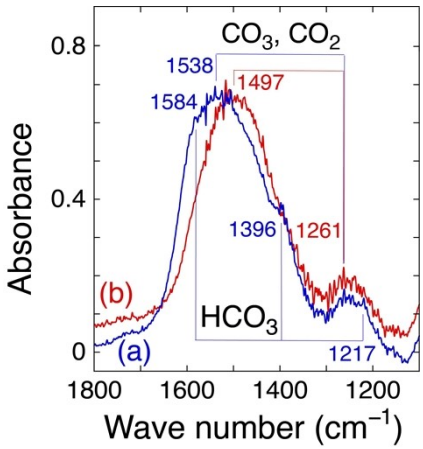

Fig. S8 FTIR spectra for Fe^0 (7.5 wt%)–ZrO_2-973R under $^{13}CO_2$ (2.3 kPa) and H_2 (21.7 kPa) (a) and during UV–Vis light irradiation (265 mW cm^{-2}; (b)).

Author contributions

TO and IA did experiments and analyzed while MS did theoretical calculations. YI made plan and wrote paper.

Acknowledgement

The authors are grateful for the financial support from the Grant-in-Aid for Scientific Research B (24K01522, 20H02834, YI) from the Japan Society for the Promotion of Science. X-ray absorption experiments were performed with the approval of the Photon Factory Proposal Review Committee (2024G067, 2022G527, 2021G546). The authors would like to thank Enago (www.enago.jp) for the language review.

ORCID of the authors

Tomoki Oyumi 0000-0002-8339-5161
Ikki Abe 0009-0008-9732-6846
Masahito Sasaki 0009-0005-1088-3382
Yasuo Izumi 0000-0001-8366-1864

References

S1 Y. Izumi, *Coord. Chem. Rev.*, 2013, **257**, 171–186.
S2 Y. Izumi, ACS Books "*Advances in CO_2 Capture, Sequestration, and Conversion*", F. Jin, L.-N. He, and Y. H. Hu, Eds., ACS Symposium Series; ACS Publications, 2015; Volume **1194**, Chapter 1, pp 1–46
S3 D. Wang, R. Huang, W. Liu, D. Sun, and Z. Li, *ACS Catal.*, 2014, **4**, 4254–4260
S4 Z. Lyu, L. Chen, J. Yin, T. Wu, K. Zhao, S. Shen, W. Wang, and L. Ge, *Separation Purification Technol.*, 2025, **354**, 129431.
S5 Z. Wang, H. Yuan, Y. Jia, L. Guo, H. Wang, and W. Dai, *Separation Purification Technol.*, 2025, **353**, 128392.
S6 X. Zhao, C. X. Tang, Q. Xu, H. Rao, D.-Y. Du, P. She, and J.-S. Qin, *J. Catal.*, 2024, **439**, 115745.
S7 A. Arash and L. Vafajoo, *Reac. Kinetics Mech. Catal.*, 2024, **137**, 1789–1803.
S8 W. Feng, P. Zhu, S. Li, J. Fu, H. Niu, Z. Ren, S. Liu, L. Zheng, D. Zhao, and J. Zhang, *J. Mater. Chem. A*, 2024, **12**, 14437–14445.

S9 D. Zhou, X. Zhang, Z. Li, J. Zhang, T. Wang, and S. Cao, *Appl. Catal. B*, 2024, **344**, 1123639.

S10 A.-Y. Lo, C.-C. Wang, J. Huang, Y.-C. Chung, and Y.-C. Chang, *J. Environ. Chem. Eng.*, 2024, **12**, 112351.

S11 T. Tian, X. Hu, Y. Li, Y. Bai, and B. Cai, *J. Environ. Chem. Eng.*, 2024, **12**, 112300.

S12 S. Gao, X. Zhao, Q. Zhang, L. guo, Z. Li, H. Wang, S. Zhang, and J. Wang, *Chem. Sci.*, 2025, **16**, 1222–1232.

S13 Y.-K. Zhang, L. Zhao, A. O. Terent'ev, and L.-N. He, *J. Mater. Chem. A*, 2025, **13**, 1407–1419.

S14 J. Wu, W. Wang, X. Chen, Q. Luo, C. Yan, Z. Jiao, and Y. Li, *Adv. Sci.*, 2024, **12**, 2409002.

S15 Y. Fang, X. Hong, and D. Chao, *Inorg. Chem. Front.*, 2024, **11**, 562–570.

S16 X. Ma, D. Li, H. Jin, X. Zeng, J. Qi, Z. Yang, F. You, and F. Yuan, *J. Colloid Interface Sci.*, 2023, **648**, 1025–1033.

S17 Q. Xu, Y. Sun, T. Lv, and H. Liu, *J. Alloys Comp.*, 2023, **954**, 170088.

S18 H. Feng, Y. Sun, Q. Xu, and H. Liu, *Appl. Catal. A*, 2023, **664**, 119350.

S19 X. He, X. Gao, X. Chen, S. Hu, F. Tan, Y. Xiong, R. Long, M. Liu, E. C. M. Tse, F. Wei, H. Yang, J. Hou, C. Song, and X. Guo, *Appl. Catal. B*, 2023, **327**, 122418.

S20 J. Li, K. Ma, C. Li, Z. Shi, and S. Feng, *ACS Appl. Mater. Interfaces*, 2023, **15**, 26619–26626.

S21Y. Wang, C. Ban, J. Meng, J. Ma, H. Zou, Y. Feng, and J. Ding, *Separation Purification Technol.*, 2023, **312**, 123379.

S22 Y. Luo, H. Han, J. Li, Q. Wang, W. Zhang, and Y. Jia, *Separation Purification Technol.*, 2023, **306**, 122734.

S23 X. Chen, Y. Li, Z. Wei, S. Li, and S. Pang, *J. Phys. Conf. Ser.*, 2023, **2587**, 012100.

S24 X.-Z. Wang, S.-L. Meng, J.-Y. Chen, H.-X. Wang, Y. Wang, S. Zhou, X.-B. Li, R.-Z. Liao, C.-H. Tung, and L.-Z. Wu, *Angew. Chem. Int. Ed.*, 2021, **60**, 26072–26079.

S25 T. Loumissi, R. Ishii, K. Hara, T. Oyumi, I. Abe, C. Li, H. Zhang, R. Hirayama, K. Niki, T. Itoi, and Y. Izumi, *Angew. Chem. Int. Ed.*, 2024, **63**, e202412090.

S26 G. Kresse and J. Furthmüller, *Phys. Rev. B*, 1996, **54**, 11169−11186.

S27 K. Hara, M. Nozaki, R. Hirayama, R. Ishii, K. Niki, and Y. Izumi, *J. Phys. Chem. C*, 2023, **127**, 1776–1788.

S28 https://doi.org/10.48505/nims.3647, provided by Dr. Y. Niwa, High Energy Accelerator Research Organization.

S29 M. Lykaki, S. Stefa, G. Varvoutis, V. D. Binas, G. E. Marnellos, and M. Konsalakis, *Catalysts*, 2024, **14**, 611.

S30 S. Biswas, C. Kundu, W. L. Ng, S. P. Samudrala, T. Jarvis, S. Giddey, and S. Bhattacharya, *J. CO_2 Utilization*, 2023, **72**, 102501.

S31 J. Kirchner, C. Zambrzycki, S. Kureti, and R. Güttel, *Chem. Ing. Tech.*, 2020, **92**, 603–607.

S32 L. Yang, L. Pastor-Pérez, J. J. Villora-Pico, S. Gu, A. Sepúlveda-Escribano, and T. R. Reina, *Appl. Catal. A*, 2020, **593**, 117442.

S33 R. Merkache, I. Fechete, M. Maamache, M. Bernard, P. Turek, K. Al-Dalama, and F. Garin, *Appl. Catal. A*, 2015, **504**, 672–681.

S34 M. A. A. Aziz, A. A. Jalil, S. Triwahyono, and S. M. Sidik, *Appl. Catal. A*, 2014, **486**, 115–122.

S35 N. Utsis, R. Vidruk-Nehemya, M. V. Landau, and M. Herskowitz, *Faraday Discuss.*, 2016, **188**, 545–563.

S36 V. I. Bogdan, A. E. Koklin, A. L. Kustov, Y. A. Pokusaeva, T. V. Bogdan, and L. M. Kustov, *Molecules*, 2021, **26**, 2883.

S37 M. V. Landau, N. Meiri, N. Utsis, R. V. Nehemya, and M. Herskowitz, *Ind. Eng. Chem. Resear.*, 2017, **66**, 13334–13366.

S38 N. Meiri, Y. Dinburg, M. Amoyal, V. Koukouliev, R. V. Nehemya, M. V. Landau, and M. Herskowitz, *Faraday Discuss.*, 2015, **183**, 197–215.

S39 C. Zambrzycki and R. Güttel, *Reactions*, 2022, **3**, 374–391.

S40 P. M. Bravo, R. Juménez, F. Devred, D. P. Debecker, C. Ulloa, and X. García, *Fuel*, 2020, **276**, 118045.

S41 X. Han, S. Huang, C. Wei, H. Liang, J. Lv, Y. Wang, M.-Y. Wang, and X. Ma, *ACS Catal.*, 2024, **14**, 18354–18364.

S42 J. M. Martín-Martínez and M. A. Vannice, *Ind. Eng. Chem. Res.*, 1991, **30**, 2263–2275.

S43 B. Kortewille, A. Springer, and J. Strunk, *Catal. Commun.*, 2021, **152**, 106286.

S44 A. F. Soares, S. H. Tatumi, R. R. Rocca, L. C. Courrol,' *J. Luminescence*, 2020, **219**, 116866.

S45 H. Zhang, T. Itoi, T. Konishi, and Y. Izumi, *J. Am. Chem. Soc.*, 2019, **141**, 6292–6301.

S46 H. Zhang, T. Itoi, T. Konishi, and Y. Izumi, *Angew. Chem. Int. Ed.*, 2021, **60**, 9045–9054.

S47 H. Zhang, T. Itoi, K. Niki, T. Konishi, and Y. Izumi, *Catal. Today*, 2020, **356**, 544–556.